(This is a sample cover image for this issue. The actual cover is not yet available at this time.)

Elastic-wave identification and extraction through array processing: An experimental investigation at the laboratory scale

Benoit De Cacqueray [a,b,*], Philippe Roux [b], Michel Campillo [b], Stefan Catheline [b], Pierre Boue [b]

[a] CGGVeritas, Massy, France. 1, rue Léon Migaux, 91341 Massy Cedex, France
[b] ISTerre, CNRS UMR 5275, Université Joseph Fourier, BP 53, 38041 Grenoble Cedex 9, France

ARTICLE INFO

ABSTRACT

The mix of body waves and surface waves is a recurrent problem for deep exploration in geophysical contexts. As surface waves represent up to 70% of the recorded energy, they hide a large part of the information coming from the sub-surface through body waves. Efforts have been made in the past to better filter or remove surface waves; however, their impact is always far from negligible, especially with strong backscattering contributions. In parallel, taking advantage of an always growing number of channels, geophysical explorations face new opportunities to enhance the quality of Earth imaging. For example, better spatial sampling is a way to better use or remove surface waves. There are compromises to find between higher spatial sampling and operational costs, even for on-field tests. In this context, surface-wave studies at the laboratory scale are a flexible way to evaluate new acquisition designs and processing. This study shows how a gel-based phantom can be used successfully to study elastic-wave mixing in the context of geophysics prospection. Small-scale experiments provide the records of thousands of traces. Using projections in the slowness/angle domain, wave separation and identification algorithms are proposed, with the goal of being able to adapt array processing to geophysical-like designs.

© 2011 Elsevier B.V. All rights reserved.

1. Introduction

The issues associated with the mixing of body waves and surface waves have been known since the beginning of exploration geophysics. Surface waves are very energetic, and they represent up to 70% of the energy recorded with sources and receivers at the Earth surface. They represent a recurrent problem for deep exploration, as they can hide a large part of the information coming from the Earth subsurface through body waves. Thus, filtering and/or modeling surface waves to cancel their impact are a constant subject of research. This takes on ever more complex simulations and tests, in particular due to the massive number of channels. Multi-component technologies, and high-density and large-area acquisition lead to simultaneous records of several tens of thousands of channels. In this context, a simple on-field test represents months of work for many people. On the other hand, simulation does not take into account all of the complexity of the field conditions. To investigate some situations, experimentation in the laboratory environment is often an attractive alternative.

Using a gel-based phantom to study wave propagation at the laboratory scale is not new. In 1927, experiments described by (Terada and Tsuboi, 1927) demonstrated the presence of Rayleigh waves in an agar-agar phantom. In medical ultrasonics, gels are widely used as *in-vitro* phantoms, to mimic human tissue. In wave physics, a lot of laboratory experiments have been carried out to study wave propagation in complex media (Fink et al., 2000). In the geophysics context, Bodet et al. (2005), Bretaudeau et al. (2008) and Campman et al. (2005) used experimental results in their studies of surface waves. On the other hand, laboratory configurations mimicking elastic-wave propagation with large amounts of data and deeper exploration (like in geophysical contexts) have seen little investigation. The main goal of this study is to realize high-density acquisition at the laboratory scale, and to investigate the correct design and/or processing to improve surface-wave and body-wave separation and identification.

In a gel with about 6% agar-agar, P-wave velocities are about 1500 m/s, and S-waves and Rayleigh waves, around 9–10 m/s. The speed ratio between P-waves and S-waves makes the P-waves nearly invisible below 1000 Hz, since their wavelength is much larger than the propagation medium. Working in gels below 1000 Hz then means dealing with shear and Rayleigh waves. With a velocity ratio of about 95%, this mix is a good approximation of the geophysical environment, where the surface-wave and body-wave velocities are similar.

Considering pulsed signals with a 500 Hz central frequency, the central wavelength is around 20 mm. With the size of an agar-agar block at 450 mm × 145 mm × 102 mm, enough distance is provided to observe wave propagation of several wavelengths between the source and receiver. The source is a circular 20-mm-diameter piezo-electric

* Corresponding author at: ISTerre, BP 53, 38041 Grenoble Cedex 9, France. Tel.: +33 4 76 63 52 43; fax: +33 4 76 63 52 52.
E-mail address: benoit.de.cacqueray@cggveritas.com (B. De Cacqueray).

transducer, and as a receiver, we use a laser vibrometer that records the time-domain vertical component of the wavefield velocity at the gel interface. The sampling frequency is 10 kHz. As illustrated in Fig. 1, we also use two remotely operated stepped motors to tilt a mirror in both directions, and thus to scan a 120 mm × 120 mm area of the gel surface with the laser vibrometer.

The two main advantages of using a laser vibrometer are: (1) to avoid any gel–sensor coupling issues; and (2) to allow very fine resolution at the gel surface. A possible drawback is the signal-to-noise ratio of the received signal. We use the Ometron VQ 500 laser-vibrometer with a full measurement range of 20 mm/s allowing a resolution of $0.02\,\mu m/s/\sqrt{Hz}$. The sampling frequency ranges from 0.5 Hz to 22 kHz. To enhance the signal quality, we emit a 3-s-duration linear chirp from the piezo source, ranging from 120 Hz to 850 Hz. After its propagation in the gel, the low-amplitude signal is received by the laser vibrometer and is cross-correlated with the emitted chirp, which leads to a 40 dB signal-to-noise ratio pulsed signal at any point of the gel surface. With a scale ratio of about 30, the 20-mm piezo size does not match the size of the vibrator trucks at the true scale. However, the objective of the laboratory-scale experiments is not to match the true-scale experimental configuration with high fidelity, but to reproduce, to some extent, the physics of wave propagation encountered during seismic exploration. In particular, the goal of this study is to deal at the laboratory scale with the ground-roll problem that appears when undesired surface waves mix with body waves. Surface waves appear as low-velocity, low-frequency, high-amplitude coherent noise that generally obscures the signal and degrades the overall data quality. Here, we show that the ground-roll problem can be alleviated through array-processing when the acquisition is performed between two arrays of sources and receivers.

This report is organized as followed: Section 2 describes the array-processing algorithm that is performed on both the source and the receiver arrays, moving from classical one-dimensional (1D) simple beamforming to the 2D double beamforming (DBF) used in this experimental configuration. Section 3 gives the advantages of the slowness representation, while Section 4 illustrates the wave-extraction abilities of DBF processing. In Section 5 the originality of the DBF extraction is discussed, before rounding things off in the conclusions in Section 6.

During this experiment, a total of 49 (sources) × 126 (receivers) = 6174 traces were recorded in the experimental configuration described in Fig. 2(a). The time-domain signals presented in Fig. 3 are a subset of the raw data after the correlation of the received signals with the emitted signal.

The wavefield is composed of a direct surface wave and several reflections, although the high number of mixed waves makes the interpretation very difficult. One way to describe these data is to split them in a 5-dimensional space $S(t, x_i, y_i, x_j, y_j)$, as we record signals as a function of time, receiver positions (defined in x_i and y_i), and sources positions (defined in x_j and y_j).

Sorting out the data space into a source-array/receiver-array space allows array processing techniques to be applied as a way to facilitate wave separation and, if possible, identification.

2. Double beamforming

Among the various array processing techniques, beamforming is widely used in multi-source and/or multi-receiver configurations. Array use started early in radio astronomy and nuclear detection, and
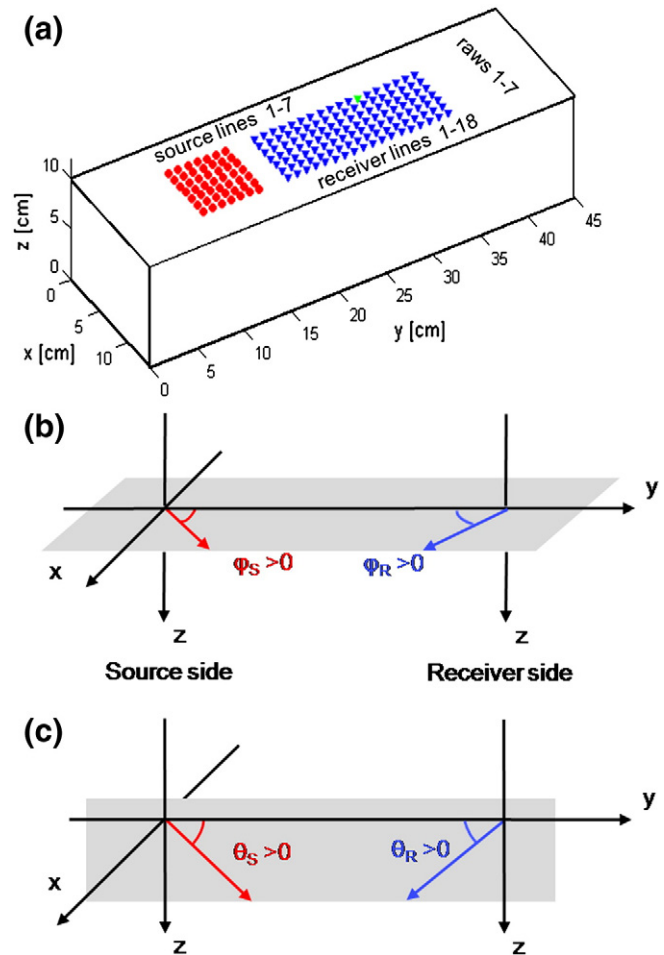
Fig. 2. Experimental design and angle definitions. (a) Experimental set-up implemented at the laboratory scale. Each red circle indicates a source point and each blue triangle a receiver point, corresponding to one piezoelectric source and one vibrometer spot, respectively. The sources and receivers are positioned on lines and rows spaced by 10 mm, for one source antenna of 7 × 7 sources (red) and 18 lines of 7 receiver points (blue). On the receiver side, a sub-antenna is defined by a square of 7 × 7 receivers. We can then consider 12 receiver sub-antennas with sub-antenna 1 as lines 1 to 7, sub-antenna 2 as lines 2 to 8, *etc*. Receiver 78 corresponds to the first of the 12th line of receivers and is highlighted in green (see Fig. 3) (b) Source and receiver azimuth angles (φ_s, φ_r). For symmetry reasons, the azimuth for the sources is taken in an inverse trigonometric sense. (c) Source and receiver incidence angles (θ_s, θ_r) with the same convention. For easier understanding of the results in Section 3, the incidence angle is defined as complementary to the classical one.
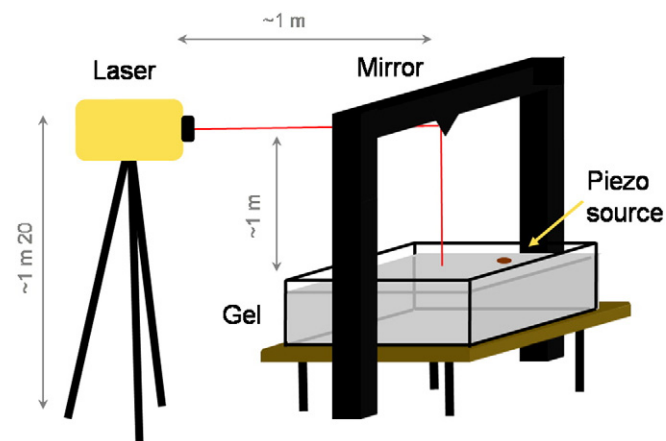

Fig. 1. Experimental configuration. The agar-agar gel is placed in a rectangular Plexiglas aquarium. The wavefield measurement is performed using a laser vibrometer pointing at the gel surface via a mirror mounted on an aluminum frame at about 1 m above the gel surface. Two high-precision motors are fixed on the mirror, to allow variable tilt for scanning of the gel surface. A circular 20-mm-diameter piezo-electric transducer fastened to the gel surface is used as a source. Pulsed signals with a frequency bandwidth ranging from 150 Hz to 850 Hz are emitted. The piezo source, the laser vibrometer, and the mirror are remotely operated by a computer.
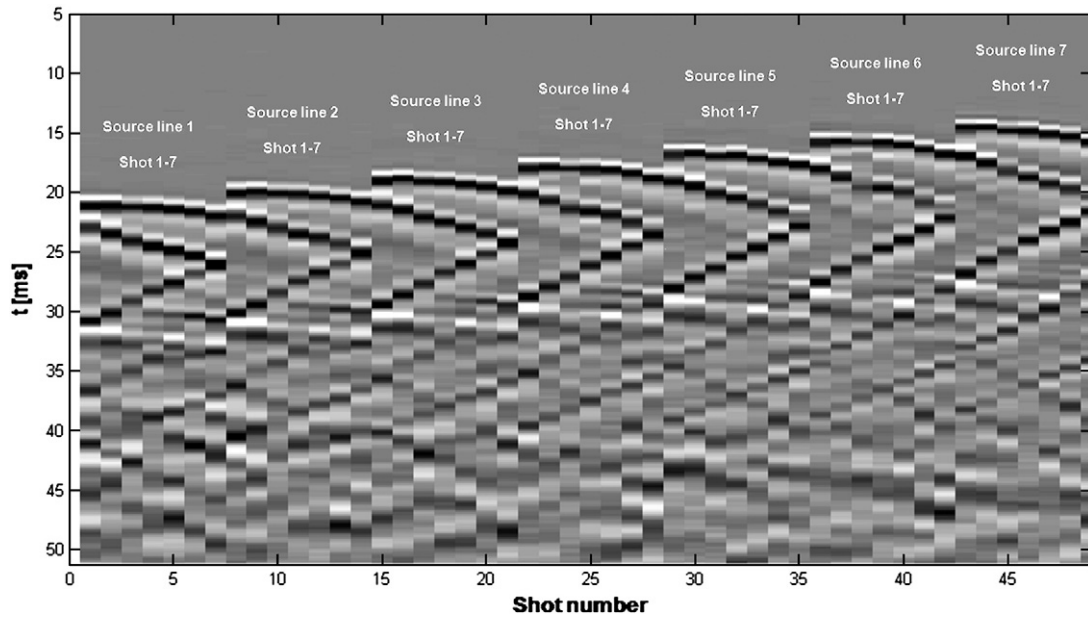
Fig. 3. Raw data after pulse compression. The horizontal axis corresponds to the shot number and the vertical axis to the recording time (ms). The image represents the data recorded at receiver 78 for the emission at point sources 1 to 49. Receiver 78 corresponds to the first of the 12th line of receivers and is highlighted in green in Fig. 2a. The wavefield is composed of a high-amplitude surface wave (the direct wave arriving between 15 ms and 22 ms), followed by several reflections on the gel edges and the bottom interface. After 30 ms, the wavefield interpretation becomes more difficult from this point-to-point representation. There are no obvious body waves in this record, since they are hidden by surface waves, as in the geophysical context.

the first applications were described by Bracewell (1957) and Carpenter (1965). The technique is now used in various domains, and more recent applications can be found in Gouédard (2008), Iturbe (2010), Roux et al. (2008) and Weber et al. (1996). The basic principle of plane-wave beamforming is the following: considering an array of receivers, the idea is to separate the incident waves by their directions of arrival, characterized by an incident angle θ_r [Fig. 2(c)]. For plane-wave beamforming to be efficient, the source–receiver distance has to be large enough with respect to the receiver separation, so that the incident waves can be considered locally as plane waves.

When dealing with broad-band signals, beamforming (also called time-delay beamforming) consists of applying a time delay to each receiver according to the arrival angle, to perform constructive interference of the recorded signal on the whole array. The beamforming transforms the recorded data on the receiver array from the position domain to the angle domain, in such a way that the wavefield intensity is focused in certain incident directions.

In our experimental configuration, beamforming on the receiver array for one given source would not be useful, since the source–receiver distance is not large enough to represent the incident field as a discrete sum of plane-wave components. In other words, the far-field hypothesis will not be fulfilled. However, using the reciprocity theorem and taking advantage of the array sources, we can also apply the plane-wave beamforming principle on the source side [Fig. 4(b)]. This means that we can select waves not only by their arrival angles, but also by their source angles. Combining beamforming on both the source and receiver arrays is known as DBF. Detailed descriptions of its applications in seismology and underwater acoustics can be found in Roux et al. (2008), Weber et al. (1996) and Weber and Wicks (1996). DBF basically projects the data space initially in the source–receiver position domain into the source–receiver angle domain through the plane-wave components of the wavefield [Fig. 4(c)]. Since the plane-wave projection is performed on both sides, there is a requirement in terms of source–receiver distance. The only assumption is that the emitted plane wave remains undistorted through its propagation in the medium. This is valid with plane reflectors in layered media. This can also be valid with scatterers, if they are far enough. In this case, the reflected wavefield coming from the

scatterer can be considered as plane waves at the receiver array. It might not be the case when strong point-like scatters are present close to the source–receiver arrays.
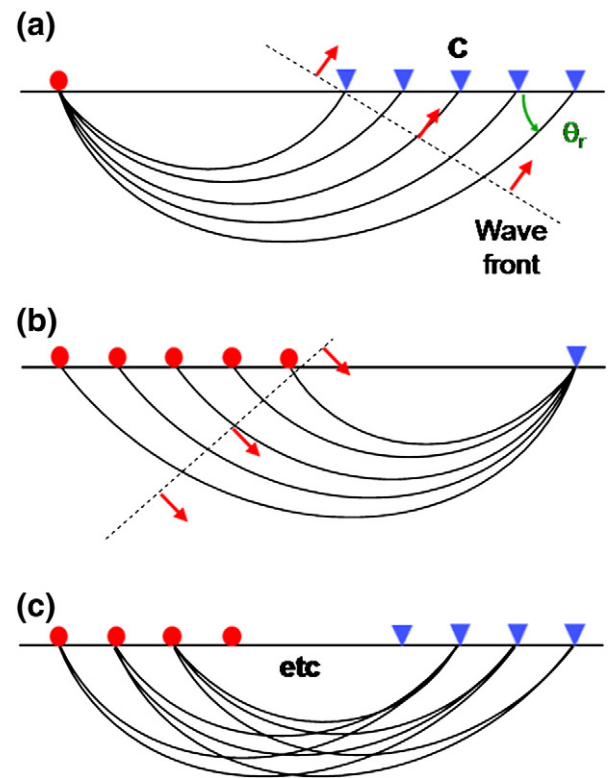

Fig. 4. Double beamforming principle. (a) Plane-wave beamforming principle from a 1D array, allowing the separation of the plane waves by their angle of arrival θ_r. (b) The reciprocity theorem allows us to perform the same separation on the source side. (c) The DBF principle considers all of the paths from every source to every receiver. Modified from Weber et al. (1996).

From the simplistic 2D geometry using linear source–receiver arrays as in Fig. 4, we go one step further, by using 2D source–receiver antennas, as shown in Fig. 2(a). In this configuration, beamforming on one array is characterized by two angles, θ_r and φ_r, the first being the incidence angle and the second the azimuth, as illustrated in Fig. 2(b), (c). Note that the incidence angle convention used here is different from the classical one. In this configuration, the time-delay to be applied on each element (x, y) of the array centered at the array center (x_c, y_c) is:

$$\tau(x, y, \theta_r, \varphi_r) = \frac{(x-x_c).\cos\theta_r.\sin\varphi_r - (y-y_c).\cos\theta_r.\cos\varphi_r}{V} \quad (2)$$

where V is the wave velocity at the surface (supposedly known, and spatially uniform on the array). For all of the computation, we only consider the intervals $[-\pi/2, \pi/2]$ for φ and $[0, \pi/2]$ for θ. Eq. (2) can be rewritten using the slowness definition ($u = \cos(\theta)/V$ with our angle convention):

$$\tau(x, y, \theta_r, \varphi_r) = u_r((x-x_c).\sin\varphi_r - (y-y_c).\cos\theta_r) \quad (3)$$

Generalizing the DBF processing for two 2D source–receiver arrays made of $N \times M$ source–receiver points finally projects the data space in the time-domain over a set of four parameters (u_r, φ_r) on the receiver array, and (u_s, φ_s) on the source array such that:

$$\tilde{S}(t, u_s, \varphi_s, u_r, \varphi_r) = \sum_{i=1}^{N} \sum_{j=1}^{M} S\left(t - \tau(x_i, y_1, u_r, \varphi_r) + \tau(x_j, y_j, u_s, \varphi_s), x_i, y_i, x_j, y_j\right) \quad (4)$$

where $S(t, x_i, y_i, x_j, y_j)$ is the signal recorded at the receiver point (x_i, y_i) that issued from the source point at (x_j, y_j). Eq. (4) shows the heavy computational cost of the DBF method. For each element of the 5-D function S, note that a double sum over the source and receiver points is performed.

Basically,

$$\tilde{S}(t_0, u_{s0}, \varphi_{s0}, u_{r0}, \varphi_{r0})$$

presents an intensity maximum for each eigenray arriving at time t_0, joining the center of the source array to the center of the receiver array, and characterized by the slowness/azimuth couples, (u_{s0}, φ_{s0}) on the source side and (u_{r0}, φ_{r0}) on the receiver side.

Due to the homogeneity of the experimental environment, we assume $u_s \approx u_r = u$ and $\varphi_s \approx \varphi_r = u$ for each eigenray. This approximation should remain valid with seismic data, as long as the velocity field at the surface is spatially homogeneous. It also significantly reduces the computational cost as computation is only performed on a 3-D subset of S given by

$$\hat{S}(t, u, \varphi) = \tilde{S}(t, u, \varphi, u, \varphi).$$

The data representation in this slowness/azimuth domain consists of searching the maxima of the $\hat{S}$ function. To represent the intensity spot corresponding to one eigenray, we project the $\hat{S}$ function into the appropriate slowness/angle space according to its arrival time. One solution is to consider the $\check{S}$ maxima for all φ at a given time. This leads to a 2D matrix:

$$\overline{S}(t, u) = \max_{\varphi}\left[\hat{S}(t, u, \varphi)\right]. \quad (5)$$

Then, we represent

$$\overline{S}(t, u)$$

in a 2D space, as shown in Fig. 5. This so-called vespagram representation was presented by Davies et al. (1971) and it is well used in seismology (Rost and Thomas, 2002).

Slowness around $u \approx 0.1$ s/m corresponds to surface-wave propagation on the gel. For $u < 0.1$ s/m, we observe body waves interacting with the bottom. The bottom image in Fig. 5 represents a subset of the DBF data, which restricts the φ values to the specular plane ($\varphi = 0$).
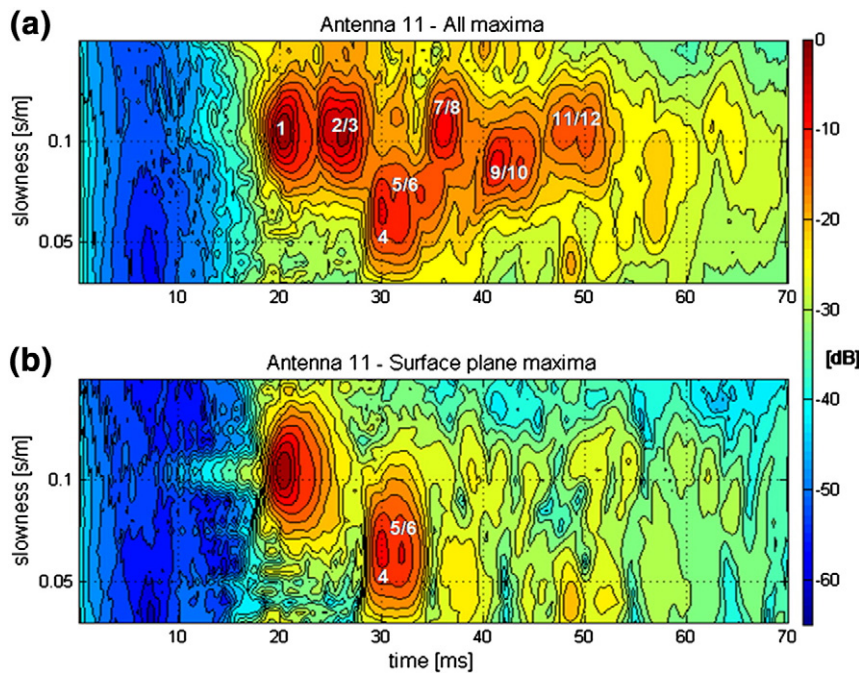
Fig. 5. Vespagram representation. (a) $\overline{S}(t, u)$ maxima *versus* time and slowness at sub-antenna 11. Each intensity peak represents one wave (or several mixed waves) arriving at the sub-antenna at time t and with slowness u. Twelve waves have been numbered in white, and these are further described in Table 1. Surface waves are characterized by a slowness of around 0.1 s/m. (b) $\overline{S}(t, u)$ maxima in the specular plane ($\varphi_s = \varphi_r = 0$), showing a powerful cleaning of the data as we remove all of the waves propagating outside the specular plane.

We note that a large part of the surface waves disappear, which corresponds to the side reflections on the gel boundaries. This is also the case for body waves that propagate outside of the specular plane. From the vespagram in Fig. 5(b), we can also estimate the surface-wave velocity. The direct surface wave corresponds to $\theta = 0$ and $V = 1/u$, from which the gel velocity V can be estimated at 9.5 m/s. In the case of the gel experiment, the vespagram provides an easy representation of twelve waves that have been numbered in Fig. 5(a) and are identified in Table 1.

3. Angle domain

If no *a-priori* information or hypothesis is available for the velocities and/or incidence angles, the vespagram provides a first study of the wavefield. Indeed, if neither V nor θ_r is known, the ratio $\cos(\theta_r)/V$ can correspond to an infinity of couple (θ_r, V).

To benefit from the θ information, the DBF processing (performed using Eq. (2)) is represented in the angle domain. For an eigenray identified on the vespagram, the arrival time, the source and receiver azimuths, and the source and receiver slowness is measured. The knowledge of V provides the incidence angle $\theta_s = \theta_r$. Then, the DBF computation can be carried out at fixed time and azimuth angles while scanning $(\theta_s$ and $\theta_r)$ values, or at fixed time and incidence angles while scanning $(\varphi_s$ and $\varphi_r)$ values. This provides (θ_s, θ_r) and (φ_s, φ_r) views, as presented in Fig. 6(b), (d) and 7(b), (d). Each eigenray is represented by an intensity spot, from which the source and receiver angles can be determined.

In Fig. 6, the direct surface wave (Table 1, wave number 1) is seen at 20 ms according to Fig. 5, with azimuth and incidence angles equal to 0° at both the source and receiver arrays. In Fig. 7, a body wave is shown (Table 1, wave number 4). As expected, we obtain azimuth angles of 0°, meaning that the wave propagates in the specular plane with incidence angles of ~67°.

Since DBF is a double plane-wave projection on the source and receiver arrays, diffraction laws can provide a theoretical prediction for each intensity spot of the DBF data at frequency ω. The analytical expression of the beamformer amplitude B (ω, θ) with a 1D linear array is:

$$B(\omega, \theta) = \frac{\sin\left(\dfrac{Nd\omega}{c(\sin\theta - \sin\theta_0)}\right)}{\sin\left(\dfrac{d\omega}{c(\sin\theta - \sin\theta_0)}\right)}, \tag{6}$$

where N is the number of elements of the antenna, d is the element spacing, c is the wave velocity, and θ_0 is the actual incidence angle.

Table 1
Wave descriptions.

| No.	Wave description
1	Direct surface wave
2	Surface wave reflection at the right edge
3	Surface wave reflection at the left edge
4	Bottom reflection
5	Bottom reflection at the right corner
6	Bottom reflection at the left corner
7	Double surface wave reflection at the left then the right edge
8	Double surface wave reflection at the right then the left edge
9	Right edge/bottom/left edge reflection
10	Left edge/bottom/right edge reflection
11	Triple surface wave reflection at the edges (right/left/right)
12	Triple surface wave reflection at the edges (left/right/left)
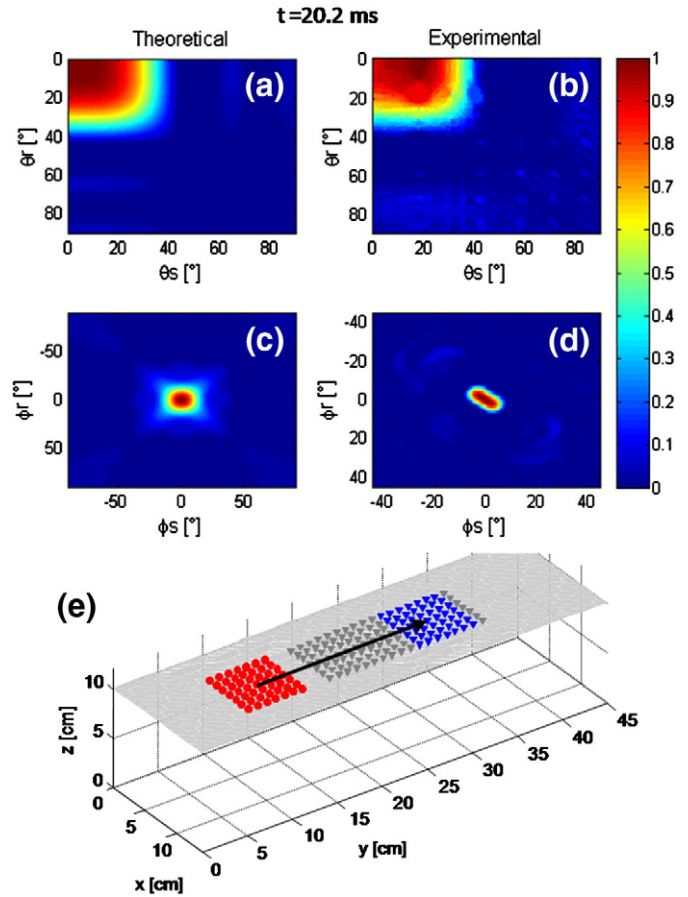
Fig. 6. Direct surface wave (wave number 1) in the angle domain at the 11th sub-antenna. (a) Theoretical beamformer intensity spot in the (θ_s, θ_r) plane. (b) Experimental DBF intensity spot in the (θ_s, θ_r) plane at time $t = 20.2$ ms and for $(\varphi_s, \varphi_r) = (0, 0)$. (c), (d) Equivalent results for the (φ_s, φ_r) plane at time $t = 20.2$ ms and for $(\theta_s, \theta_r) = (0, 0)$. (e) Source array (red) and receiver subarray (blue) in the propagation plane (gray). Black arrow, the eigenray path. As expected for a surface wave, the intensity spot is maximal for low values of incidence and azimuth angles.

This expression can be easily generalized to both incidence and azimuth angles for 2D source and receiver arrays. In the 2D geometry, the beamformer amplitude in the (θ_s, θ_r) space is:

$$B(\omega, \theta_s, \theta_r) = B(\omega, \theta_s).B(\omega, \theta_r) \tag{7}$$

and for the azimuths (φ_s, φ_r):

$$B(\omega, \varphi_s, \varphi_r) = B(\omega, \varphi_s).B(\omega, \varphi_r). \tag{8}$$

For comparison, we present in Figs. 6(a), (c) and 7(a), (c) the corresponding theoretical beamformer patterns. We observe good agreement between the predicted intensity spots and the DBF results for both the direct surface wave and the bottom-reflected body wave.

Note also that DBF provides an array gain that depends on the number of sources and receivers. With N sources and M receivers by sub-antenna, the gain is $\sqrt{N.M} = 49$, or equivalent to about 34 dB in our experiment.

Finally, Fig. 8(a) and (b) illustrates the DBF intensity spot in the angle space for each of the 12 receiver sub-antennas and the surface wave that bounces once on the edge of the gel (Table 1, wave number 2). On the (θ_s, θ_r) views, the intensity is slightly decreasing when the source–receiver distance (or offset) increases. On the (φ_s, φ_r) views, two spots are visible,
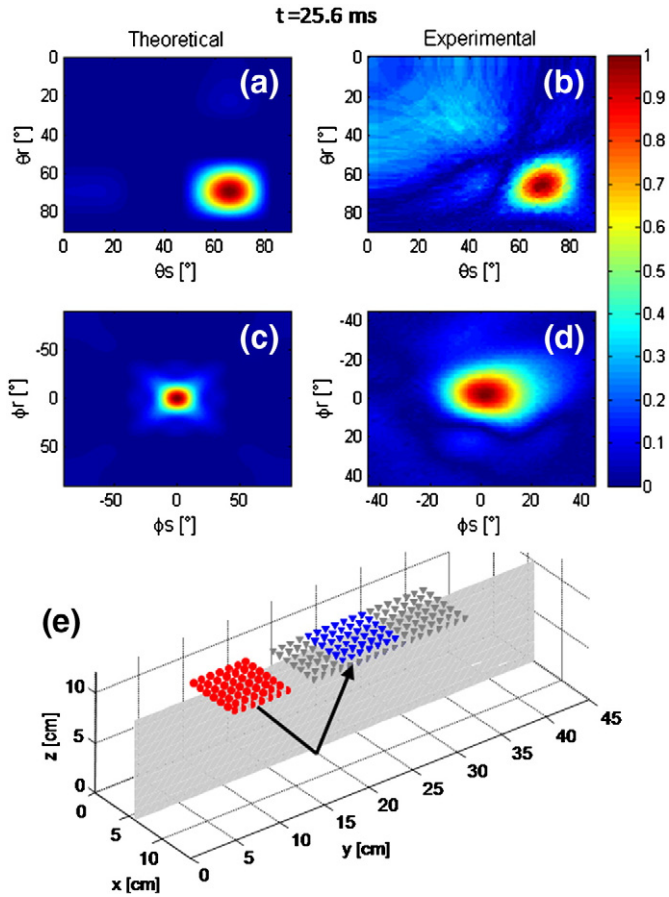
Fig. 7. Bottom-reflected body wave (wave number 4) in the angle domain at the 5th sub-antenna. (a) Theoretical beamformer intensity spot in the (θ_s, θ_r) plane. (b) Experimental DBF intensity spot in the (θ_s, θ_r) plane at time $t = 25.6$ ms and for $(\varphi_s, \varphi_r) = (0°, 0°)$. (c), (d) Equivalent results for the (φ_s, φ_r) plane at time $t = 25.6$ ms and for $(\theta_s, \theta_r) = (69°, 66°)$. (e) Source array (red) and receiver subarray (blue) in the propagation plane (gray). Black arrow, the eigenray path. The eigenray is characterized by a null azimuth angle. Incidence angles vary with the sub-antenna position. For sub-antenna 5, the incidence angle is about 67.5°.

which correspond to the two reflections on both the left and right edges of the gel. The second spot appears less energetic, since the arrival times of the two reflections are not identical. The angle-*versus*-offset figures show very concentrated intensity spots. This demonstrates the DBF ability to separate the different waves, even when they overlap in time. Compared to the classical time-offset representation (Fig. 3), the angle domain representation provides a deeper analysis of the wavefield complexity.

4. Wave extraction

From the DBF representation, different waves can be extracted by selecting a subset of the 5-dimension matrix in the angle domain. To go back from the $(t, \theta_s, \varphi_s, \theta_r, \varphi_r)$ angle domain into the (t, x_i, y_i, x_j, y_j) position space, we simply apply time-delays as in Eq. (2), although the signs of the delays are reversed:

$$S\left(t, x_i, y_i, x_j, y_j\right) = \sum_{s=1}^{P} \sum_{r=1}^{Q} \tilde{S}\left(t + \tau(x_i, y_i, u_r, \varphi_r) - \tau\left(x_j, y_j, u_s, \varphi_s\right), \theta_s, \varphi_s, \theta_r, \varphi_r\right). \quad (9)$$

In Fig. 9(a), the raw data between the source array center and the center of the 12-receiver subarrays are represented prior to any beamforming. The four other panels in Fig. 9 represent waves after DBF
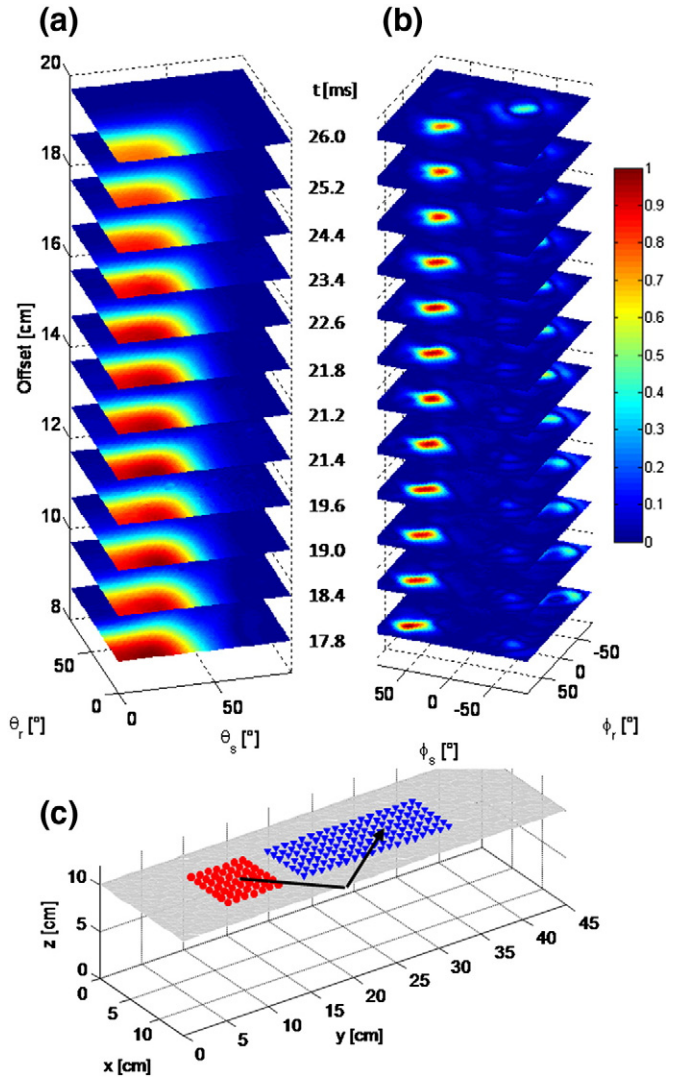

Fig. 8. DBF representation in the angle domain for the edge-reflected surface waves (wave number 2) and for the receiver sub-antennas 1 to 12. (a) Slice gather of (θ_s, θ_r) planes for offsets 1 to 12 at azimuth angles $(\theta_s, \theta_r) = (0, 0)$. Arrival times are given in bold for each sub-antenna. (b) Slice gather of (φ_s, φ_r) planes for offsets 1 to 12 at incidence angles $(\theta_s, \theta_r) = (0, 0)$. (c) Source array (red) and receiver subarray (blue) in the propagation plane (gray). Black arrow, the eigenray path; according to the arrow, the intensity spot corresponds to positive values of φ_s and φ_r. We note a second spot with lower intensity for negative values of φ_s and φ_r, which corresponds to a second reflection at the opposite side of the Plexiglas aquarium. As the design is not completely symmetrical, this reflection arrives a bit later with a delayed intensity maximum.

extraction: the direct surface wave (wave number 1; Fig. 9(b)); the surface wave after one reflection on the right edge (wave number 2; Fig. 9(c)); the body wave with one reflection on the bottom (wave number 4; Fig. 9(d)); and the surface wave after two reflections on the edge (wave number 7; Fig. 9(e)). One noticeable result is that the separation in the angle domain is efficient, with the five waves arriving between the times of 28 ms and 38 ms [Fig. 5(a)] with different azimuth/incident angles. For the direct surface wave, we observe constant wavelet amplitude *versus* offset distance. This arises as the beamforming process performs a plane-wave projection both on the source and the receiver arrays. As such, the geometrical attenuation of magnitude $1/r$ for the body waves and $1/\sqrt{r}$ for the surface wave disappears. Nevertheless, a slight amplitude decrease is still visible. For
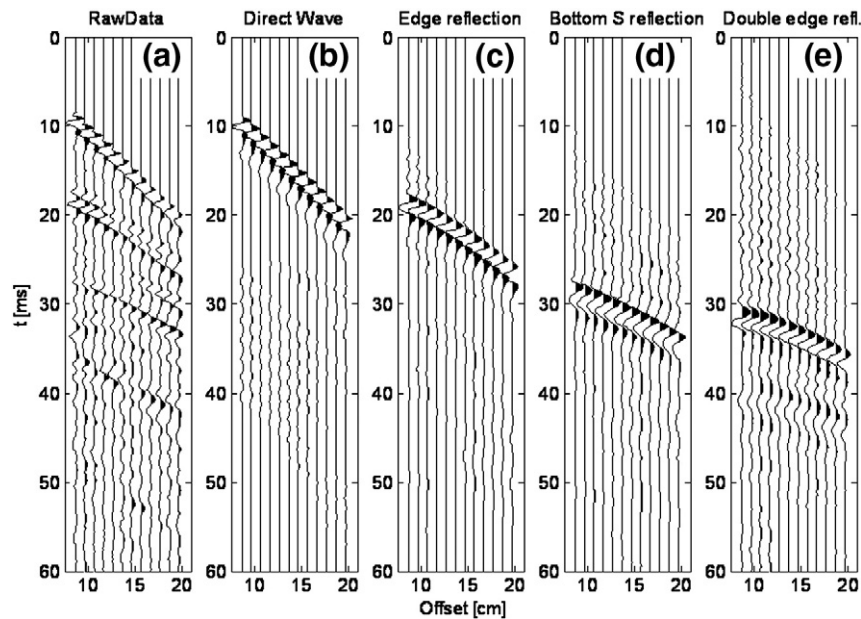
Fig. 9. Wave extraction after DBF processing. (a) Raw data for offset 8.7 cm to 19.7 cm without DBF. (b–e) After extraction using DBF: (b) direct surface wave (wave number 1); (c) surface wave with simple reflection at the edge of the Plexiglas aquarium (wave number 2); (d) body wave with bottom reflection (wave number 2); and (e) surface wave with double reflection on the edges of the Plexiglas aquarium (wave number 7).

example, the direct surface wave represented in Fig. 9(b) shows a peak amplitude loss of 1.4 dB between the first and the last antenna, which are spaced by 11 cm. This loss is due to the attenuation in the medium and can be compared with the Voigt theoretical predictions given by Catheline et al. (2004). With a shear Lame coefficient of 100 kPa and a shear viscosity coefficient of 1.0, the attenuation is 3.15 m^{-1} at 400 Hz, which represents 1.5 dB for 11 cm. As expected, the noise level increases for the later arrivals, since these waves are less energetic and are more impacted by the ambient noise and/or the residuals of the other waves. Finally, the DBF results in the angle domain provide a clear physical insight into the data. Providing that the angle resolution is fine enough, all of the different waves are well isolated.

From the experimental results in Figs. 5 to 9, a methodology can be derived for wave identification and extraction using DBF. If the medium velocity is unknown, as in seismology or in geophysics, the first step consists in the vespagram representation of the DBF field. This allows the recovery of arrival times and azimuth angles at reasonable computational cost. If the medium velocity is known – as in oceanography or with laboratory gel-based phantoms – or if some hypotheses are possible for the velocity field, the DBF result in S(t, θ$_s$, φ$_s$, θ$_r$, φ$_r$) can be calculated from Ŝ(t, u, φ) at a lower computational cost.

5. Discussion

The DBF method is part of the large field of signal–noise separation methods (considering that 'noise' can include interfering wavefields or not). Incoherent noise reduction using f-x deconvolution (Canales, 1984) or f-x projection filtering (Soubaras, 1994) has seen great success in the geophysical prospection industry. In Glangeaud and Mari (1994) and Mars et al. (2004), three families of wave separations were presented: (a) template methods using filtering masks, like f-k and tau-p (Yilmaz, 2002); (b) inversion methods using parameter estimations of the wave characteristics before separation (Esmersoy, 1988); and (c) filtering methods based on spectral matrix estimations using, for example, spectral value decomposition (Mars et al., 2004; Spitz, 1991).

The DBF method can be classified as part of the first family. As for the f-k method, a relatively fine spatial sampling is needed. The beamforming method is comparable with the tau-p method – or the slant-stack, as tau-p and radon often refer to inversion processes – with sliding sets of data. The particularity of beamforming is to project data in the angle domain and provide a more intuitive representation. Another characteristic of DBF is to use 2D antennas for complete characterization of the eigenrays. Further studies will focus on operational constraints with lower spatial sampling and/or array sizes. Combinations with existing methods can also be investigated.

6. Conclusions

This study demonstrates the use of array processing to efficiently separate surface and body waves in the context of geophysics exploration. The experimental demonstration was conducted at the laboratory scale in an agar-agar gel in which the point-to-point elastic wavefield was recorded between a set of piezo-electric sources and a laser vibrometer scanning an extended surface. We have shown the capabilities of DBF in this experimental environment, which reveals that it is very powerful for surface-wave and body-wave separation and identification. In practical applications, DBF processing is limited by the heavy computation of a multidimensional matrix. However, this computation can be replaced by a slowness approach, through the calculation of a vespagram at a lower computational cost, from which waves can also be separated and identified. Slowness is interesting when the velocity field is unknown, as the first step to separate waves and to recover the DBF results while reducing computational complexity. In all cases, slowness computation gives comprehensive wave representation to complement angle-domain views. These laboratory scale experiments underline the DBF processing capability and suggest further experiments to see how it can help for geophysical exploration. Diffusive layers and/or scatterers should be considered in priority in order to simulate weathering zone heterogeneities faced in geophysical contexts.

References

Bodet, L., Van Wijk, K., Bitri, A., Abraham, O., Grandjean, G., Cote, Ph., Leparoux, D., 2005. Surface wave dispersion inversion when the 1D assumption breaks down. Journal of Environmental and Engineering Geophysics 10 (2), 151–162.

Bracewell, R.N., 1957. Antenna problems in radio astronomy. IRE Natl Convention Record 5, 68–71.

Bretaudeau, F and Leparoux, D. and Abraham O., Small scale adaptation of the seismic full waveform inversion method — application to civil engineering applications, ACOUSTICS 2008.

Campman, Xander H., van Wijk, Kasper, Scales, John A., Herman, Gérard C., 2005. Imaging and suppressing near-receiver scattered surface waves. Geophysics 70 (2), V21–V29. doi:10.1190/1.1884831.

Carpenter, E.W., 1965. An historical review of seismometer array development. Proceeding of IEEE 53, 1816–1821.

Catheline, S., Gennisson, J.-L., Delon, G., Fink, M., Sinkus, R., Abouelkaram, S., Culioli, J., 2004. Measurement of viscoelastic properties of homogeneous soft solid using transient elastography: an inverse problem approach. The Journal of the Acoustical Society of America 116 (6), 3734–3741.

Davies, D., Kelly, E.J., Filson, J.R., 1971. Vespa process for analysis of seismic signals. Nature Physical Scienc 232, 8–13.

Velocity estimation from offset VSPs using direct P- and converted SV-waves., Esmersoy C., 58th Ann. Internat. Mtg., Soc. Expl Geophys., Expanded Abstracts — 1988, pages 538–541.

Fink, M., Cassereau, D., Derode, A., Prada, C., Roux, P., Tanter, M., Thomas, J.-L., Wu, F., 2000. Time-reversed acoustics. Reports on Progress in Physics 63, 1933–1995.

Glangeaud, F., Mari, J.L., 1994. Wave separation. Part two: applications. Oil and gas sciences and technologies. IFP Energies nouvelles 49, 21–61.

Techniques de corrélations: aspects méthodologiques et applications à la sub-surface, Gouédard P., UJF — PhD thesis 2008.

Tomographie acoustique haute résolution dans un guide d'onde océanique, Iturbe I – UJF – PHd thesis 2010.

Random noise reduction, Canales, L.L., 54th Ann. Internat. Mtg., Atlanta, Soc. Expl Geophys., Expanded Abstracts — 1984, pages 525–527.

Signal-preserving random noise attenuation by the f–x projection, Mars, J. and 441 Glangeaud, F. and Lacoume, J.L. and Fourmann, J.M. and Spitz, S., 56th Ann. Internat. 442 Mtg., Soc. Expl Geophys., Expanded Abstracts — 1987, pages 489–492.

Roux, Ph., Cornuelle, B.D., Kuperman, W.A., Hodgkiss, W.S., 2008. The structure of raylike arrivals in a shallow-water waveguide. Acoustical society of America 124 (6), 3430–3439.

Rost, S., Thomas, C., 2002. Array seismology: methods and applications. Review of Geophysics 40 (3), 1008. doi:10.1029/2000RG000100.

Signal-preserving random noise attenuation by the f–x projection, Soubaras, R., 64th Ann. Internat. Mtg., Soc. Expl Geophys., Expanded Abstracts — 1994, pages — 1576–1579.

Spitz, S., 1991. Seismic trace interpolation in the f-x domain. Geophysics 56, 785–794.

Experimental studies on elastic waves, Terada, Torahiko and Tsuboi, Chuji, Reprinted in Seismic Physical Modeling from Bulletin of the Earthquake Research Institue, 1927, Vol. 3, pages 55–65 with permission of Univ. of Tokyo, Geophysics reprint series 1994 no 15, pages 56–66

Weber, M., Davis, J.P., Thomas, C., Krüger, F., Scherbaum, F., Schlittenhardt, J., Körnig, M., 1996. The structure of the lowermost mantle as determined from using seismic arrays. In: Boschi, E., Ekström, G., Morelli, A. (Eds.), Seismic Modeling of the Earth's Structure. Instit. Naz. di Geophys, Rome, p. 399.

Weber, M., Wicks Jr., C.W., 1996. Reflections from a distant subduction zone. Geophysic. Res. Let 23, 1453–1456.

Yilmaz, O., 2002. Seismic Data Processing 1 and 2.